

Application of a Momentum Source Model to the RAH-66 Comanche FANTAIL

Tor A. Nygaard* and Arsenio C. Dimanlig*

ELORET Corp., Ames Research Center, Moffett Field CA 94035

Edward T. Meadowcroft†

Boeing U.S. Army Programs and Military Rotorcraft, Ridley Park, PA 19078

A Momentum Source Model has been revised and implemented in the flow solver OVERFLOW-D. In this approach, the fan forces are evaluated from two-dimensional airfoil tables as a function of local Mach number and angle-of-attack and applied as source terms in the discretized Navier-Stokes equations. The model revisions include a new model for forces in the tip region and axial distribution of the source terms. The model revisions improve the results significantly. The Momentum Source Model agrees well with a discrete blade model for all computed collective pitch angles. The two models agree well with experimental data for thrust vs. torque. The Momentum Source Model is a good complement to Discrete Blade Models for ducted fan computations. The lower computational and labor costs make parametric studies, optimization studies and interactional aerodynamics studies feasible for cases beyond what is practical with a Discrete Blade Model today.

Nomenclature

c	rotor blade chord
C_l	lift coeff. = $L/0.5\rho_\infty U_\infty^2 c$
C_T	thrust coeff. = $Fz/\rho_\infty V_{tip}^2 \pi R^2$
C_Q	torque coeff. = $Mz/\rho_\infty V_{tip}^2 \pi R^3$
FM	figure of merit = $C_T \sqrt{C_T}/2C_Q$
F_z	thrust force
h_0	stagnation enthalpy
L	lift force per unit span
M	Mach number
M_z	fan torque
p	pressure
Re	Reynolds number
R	rotor radius
U	air speed
V_{tip}	rotor tip speed
y^+	turbulent wall coordinate
α	angle-of-attack
δ	tip gap
γ	thrust augmentation factor = C_T/C_{Tfan}
ρ	air density
$\theta_{.75}$	collective pitch angle at 75% radius

Subscripts

∞	freestream
$disk$	rotor disk location
tip	rotor blade tip
z	axial direction, positive out inlet
ψ	tangential direction
fan	fan contribution

Introduction

Computational Fluid Dynamics (CFD) modeling of helicopters can be applied with different levels of detail. In a Navier Stokes Discrete Blade Model (DBM), the individual blades moving relative to the fuselage are included. This requires significant computer resources. For the RAH-66 Comanche, the five main rotor blades and eight tail rotor blades require more than three times the number of grid points used for the fuselage. The fast spinning tail rotor limits the time step to approximately one tenth of what would be used in a simulation without the tail rotor.

For many applications, such as the evaluation of helicopter tailfan control authority, the unsteady behavior of the individual fan blades is not the primary concern. In this case, one approach is to treat the rotor in a time-filtered manner. The rotor then appears to be a disk, which can be seen as a limiting case with an infinite number of blades. The interaction between the flow field and the rotor is modeled, and the moving blade geometry is removed from the

*Research Scientist

†Aerospace Engineer

problem. This saves labor cost for grid generation, computational effort in terms of the number of grid points, and potentially allows steady state techniques to be employed. A simplified treatment of the rotors on the RAH-66 Comanche can potentially bring down the computational cost by more than a factor 30. The rotor configurations can easily be changed, since this only involves changing parameters in tables rather than generating new rotor grids.

Several authors have applied actuator disk and momentum source models (MSM) to helicopter tail ducted fans. Rajagopalan and Keys¹ performed axisymmetric steady laminar Navier-Stokes computations of the RAH-66 Comanche FANTAILTM in hover and sideward flight with a momentum source approach. The flow solver utilized non-body-fitted grids. Alpman, Long and Kothman² performed unsteady 3D Euler computations of the RAH-66 Comanche FANTAILTM in forward flight with an actuator disk model with uniform forcing. The flow solver utilized unstructured body-fitted grids.

The results presented in this paper are from Reynolds-Averaged Navier-Stokes (RANS) computations with the flow solver OVERFLOW-D fully coupled with a MSM. OVERFLOW-D utilizes body-fitted structured overset grids. The MSM is based on a pressure disk and momentum source model that was originally used with an incompressible flow solver for unducted helicopter rotors.³ The MSM allows variable forcing both radially and tangentially, with the aerodynamic forces taken from airfoil tables. The validation of the MSM with OVERFLOW-D for ducted fan cases reveals issues that are specific to this particular application. Detailed comparisons with recent DBM results by Ruzicka and Strawn⁴ for the RAH-66 Comanche FANTAILTM proves crucial for diagnosing the problems, and for revision of the MSM for ducted fan applications. The new features of the MSM significantly improve the computations. Finally, comparisons are made between RANS/MSM, RANS/DBM and experimental results for the RAH-66 Comanche FANTAILTM.

FANTAIL Configuration and Testing

Introduction

The RAH-66 Comanche is an armed reconnaissance and light attack helicopter, including air combat and nap of earth operations, for day, night and adverse weather conditions. The anti-torque system is a fan-in-fin, designated the FANTAILTM. The FANTAILTM is similar to the Sikorsky S-67 Blackhawk fan-in-fin flown in 1974 and the Aerospatiale Fenestron.⁵ Compared to conventional tail rotors, the FANTAILTM has superior survivability characteristics. In addition,

the FANTAILTM requires less power to hover than conventional tail rotors with similar disk loadings.⁶ The FANTAILTM configuration was developed in a series of wind tunnel tests: two-dimensional airfoil tests; a 1/3 scale test of FANTAILTM inlet and exhaust lip radii; a scale powered model of the complete helicopter configuration, including interaction effects of the fuselage and main rotor on the FANTAILTM and empennage; scale and full scale powered tests of the FANTAILTM; and, finally, the H-76 FANTAILTM Demonstrator flight test. These data were combined with simulation studies, S-67 test data and analyses during the trade studies to refine the FANTAILTM design.

Scale Wind Tunnel Test Description

The scale wind tunnel test was conducted in the Boeing V/TOL Wind Tunnel from July through November 1989.⁷ The purpose of this test was to determine aerodynamic and acoustic characteristics of the FANTAILTM anti-torque device as well as its tail and closure configurations. This was done on a nearly full scale FANTAILTM to minimize scaling requirements. The main test objectives were to:

1. Obtain performance and loads characteristics of the FANTAILTM during hover; low speed; quartering, sideward and rearward flight; and high speed forward flight.
2. Determine aerodynamic characteristics with tail on and off.
3. Quantify fan fairing and momentum drag.
4. Establish control derivatives and control power.
5. Determine fan dynamic characteristics.
6. Determine fan acoustic characteristics.

The FANTAILTM is an 8 bladed rotor with a rectangular planform, NACA 64 series airfoils and minus seven degrees of twist from hub to tip. The 64 series airfoils provide the required aerodynamic characteristics over the design envelope, while minimizing development risk. The minus seven degrees of twist provides optimal performance, while maximizing responsiveness as the rotor transitions from negative to positive collectives. The untapered planform minimizes manufacturing risk. The number of blades is considered optimal for acoustics and durability. The fan tip speed is based on acoustics. Fan solidity was chosen based on performance and the turn to target maneuver requirement.

The FANTAILTM duct is critical to achieving high performance efficiency. In hover the duct allows the

fan diameter to be smaller than a conventional tail rotor for the same power required. Negative static pressure on the duct inlet produces approximately 50% of the FANTAILTM thrust. The duct depth was optimized to maximize hover performance while minimizing profile drag in forward flight. The final duct configuration is the minimum depth required to house support structure and achieve acoustics goals. The duct divergence angle of 5 degrees (half angle) was chosen to prevent premature flow separation along the wall and to achieve performance goals. A sharp exit radius at the duct outlet was required for best static performance, but negative thrust and forward flight performance were compromised.

The BVWT is a closed-circuit, single-return wind tunnel capable of airspeeds over 200 knots. The test section has a 20 ft by 20 ft cross section with solid walls. The test section walls and floor can be removed for hover testing. During hover testing the model was yawed 110 deg in the left sideward flight direction, allowing the fan wake to blow in the upstream direction. The North wall and roof were removed and the South wall and floor left in the test section. Figure 1 shows the test section and the wind tunnel model. The test model was a 75% scale model consisting of

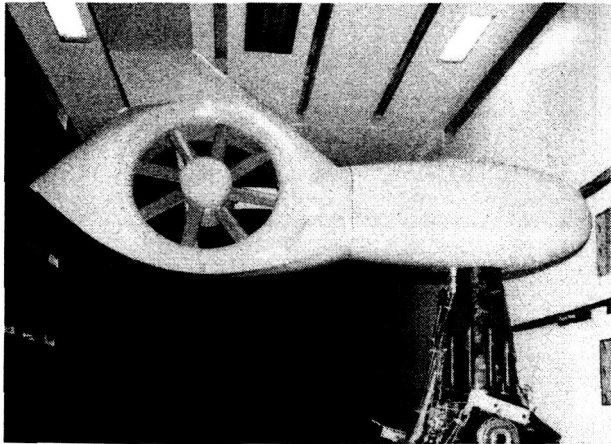


Fig. 1 BVWT test section and wind tunnel model.

a tailboom, fan, fan gearbox, slipring, fan duct and shrouds, canted vertical tail, and a high mounted horizontal tail. The fan tip speed was equal to its full scale value. The blade twist schedule was the same as full scale. The blade thickness and taper differed from full scale. The blade tip to duct clearance was 80% of the full scale clearance. A strain-gauged six component balance measured total forces on the entire model. The gauge time stream data is processed for the mean and minimum and maximum unsteady values. A nose fairing covered the balance and drive shafting. The nose fairing was attached to the ground side of the

balance. A gap existed between the grounded nose and the shroud on the live side of the balance. Flex couplings were installed in the drive shaft and strain gauged to measure torque. To improve accuracy, a torque bridge was added to the drive shaft near the ground end of the balance. Many pressure taps were installed throughout the model fairings, mainly on the inlet side duct lips and the vertical tail. A limited set of pressure taps were installed on the exhaust side. The pressure measurement system was a PSI type, consisting of pressure taps connected to small diameter air tubes, which were connected to individual transducers in a base module. An algorithm converted the pressure measurements into derived shroud fairing thrust. Isolated fan thrust was derived from balance-measured total system thrust minus pressure-derived shroud thrust.

Full Scale Hover Whirl Tower Test Description

The full scale, whirl tower hover test was conducted at the Sikorsky Aircraft 2,000 HP Tail Rotor Precession test stand from June 1995 to January 1996.⁸ The purposes of the FANTAILTM whirl tower test were to:

1. Demonstrate functional adequacy, structural integrity, and airworthiness of the FANTAILTM prior to first flight.
2. Obtain aerodynamic hover performance data at various tip Mach numbers.
3. Define the blade to duct clearance. Blade tip to duct clearance is measured using a blade at flat pitch at the 50% blade chord.
4. Evaluate overall noise signature of the fan in the far acoustic field.

The test article was a complete full scale FANTAILTM rotor/gearbox and shroud assembly. None of the vertical and horizontal tail was assembled. Figure 2 shows the whirl tower rig. All performance testing was conducted with the FANTAILTM tip path plane oriented parallel to freestream winds. All struts and fairings (including gearbox, gearbox support struts, spinner, and driveshaft cover) in the duct were installed. Torque was measured at the test facility gearbox output shaft. System (fan and shroud) thrust was measured by a load cell in the test facility. An array of pressure taps was installed on the inlet side duct lips. Pressure transducers were used to measure the vacuum pressure at small holes in the duct. An algorithm multiplying the pressure measurements by weighted surface areas derived shroud thrust. Isolated fan thrust is derived as total system thrust minus derived shroud thrust. The scale and whirl tower tests

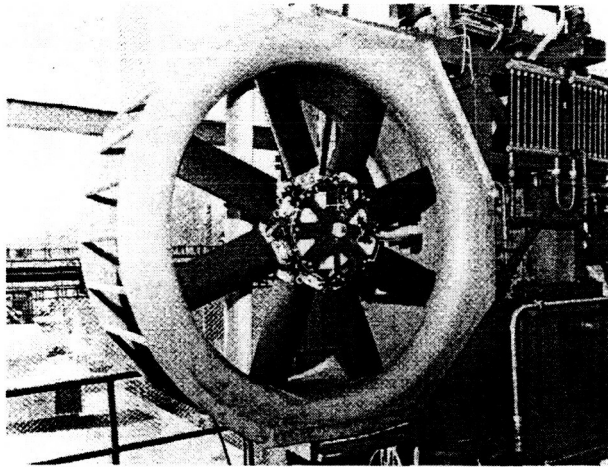


Fig. 2 Whirl tower rig.

were performed on different models at different scales in different test facilities, yet the aerodynamic performance data between the two tests are almost identical.

Computational Model Description

A near-body and off-body domain partitioning method⁹ is used here as the basis of discretization. In this approach, the near-body portion of a domain is defined to include the surface geometry of all bodies being considered and the volume of space extending a short distance away from the respective surfaces. The near-body grids are body-fitted. The construction of near-body grids and associated intergrid connectivity is a classical Chimera-style decomposition of the near-body domain. It is assumed that near-body grids provide grid point distributions of sufficient density to accurately resolve the flow physics of interest (i.e., boundary-layers, vortices, etc.) without the need for refinement. This is a reasonable constraint since near-body grids are only required to extend a short distance away from body surfaces.

The off-body portion of the domain is defined to encompass the near-body domain and extend out to the far-field boundaries of the problem. The off-body domain is filled with overlapping uniform Cartesian grids of variable levels of refinement. The grid spacing approximately doubles for each successive level of off-body grids.

The base-line grid system for the Comanche FANTAILTM wind tunnel model is shown in Figure 3. This grid system has four body-fitted near-body grids. For the axi-symmetric MSM computations presented in this paper, the Cartesian off-body grid system has been replaced with one box grid. The flow solver is switched off for irrelevant points, such as the boxgrid points well inside near-body domain. This is shown on the figure as a hole in the box grid.

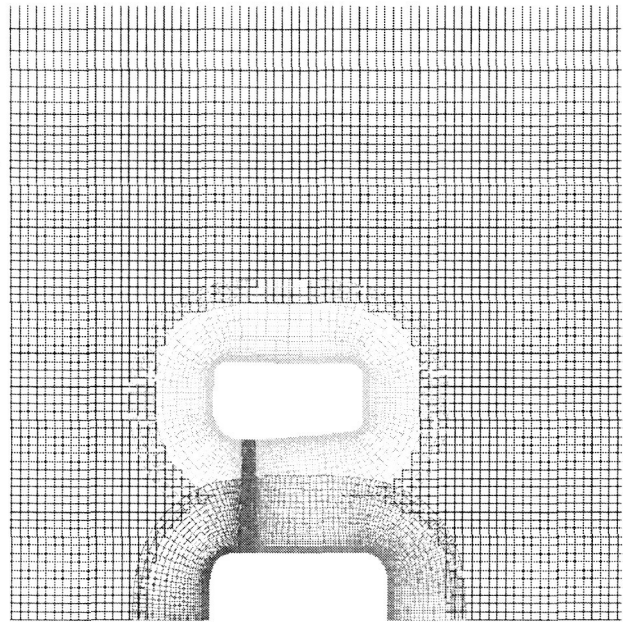


Fig. 3 Baseline grid system.

The set of simulations presented in this paper are products of the OVERFLOW-D¹⁰ code. OVERFLOW-D is based on version 1.6au of the well known NASA OVERFLOW¹¹ code, but has been significantly enhanced to accommodate moving body applications. The OVERFLOW-D enhancements represent in-core subroutine actuated operations and include the following capabilities:

1. On-the-fly generation of off-body grid systems.
2. Message Passing Interface (MPI) enabled scalable parallel computing.
3. Automatic load balancing.
4. Aerodynamic force and moment computations.
5. General 6-degrees-of-freedom model.
6. Rigid-body relative motion between an arbitrary number of bodies.
7. Domain connectivity.
8. Solution error estimation.

In cases that involve relative motion between configuration components, body dynamics and domain connectivity are addressed at each time-step. In order for solution information to be correctly exchanged between grids during the simulation, the domain connectivity solution must also be continuously updated.

This is accomplished automatically by OVERFLOW-D. The OVERFLOW-D processing rate for static geometry viscous flow applications is about $15\mu\text{sec}$ per grid-point per time-step (300MHz processor). For moving-body problems, the processing rate is somewhat problem dependent, but generally falls in the bounds of 15 to $18\mu\text{sec}$ per grid-point per time-step.

OVERFLOW-D accommodates problem sizes of more than 2 million grid-points per 1 gigabyte of memory. Maximum parallel efficiency ($> 90\%$) is realized when the fewest number of processors that can accommodate a given problem in core memory are selected. OVERFLOW-D can efficiently ($> 70\%$) make use of larger numbers of processors for a fixed problem size when each processor assumes the load of at least 250 thousand points. Load balancing is an automatic function of OVERFLOW-D.

OVERFLOW-D has recently been supplemented with a pressure disk/MSM.³ The MSM is based on a pressure disk and momentum source model that was originally used with an incompressible flow solver for unducted helicopter rotors. The interaction between the rotor and the flow field can be modeled in two different ways. In both approaches, the force vectors per unit length of the blades are obtained from airfoil tables of aerodynamic force coefficients. The coefficients are interpolated as a function of local Mach number and angle-of-attack, allowing variations both radially and tangentially on the rotor. The effects of non-uniform induced velocities are, therefore, taken into account. The time filtered force vectors at each position on the rotor disk acting back on the flow field are split into axial, radial and tangential components. In the pressure disk approach, the interactions between the axial force components and the flow field are then modeled with corresponding pressure jumps across the rotor disk. The interactions between the tangential force components and the flow-field are modeled with jumps in tangential velocity across the disk, evaluated by momentum theory. In the MSM approach, the forcing of the flow-field is achieved by applying the time filtered forces as body force source terms in the discretized Navier Stokes equations.

The pressure disk and momentum source models are both fully coupled with the flow field. At each time step of the flow solver, the local induced velocities are taken into account when evaluating the forces acting on the rotor blades. The corresponding forces acting from the blades back on the flow field influence the induced velocities evaluated by the flow solver, which again influence the forces acting on the blades in the next time step.

The flow solver configuration used for the Navier-Stokes computations in the present work is the following:

1. Central differences, second order in space.
2. ARC3D 3-factor diagonal implicit time-stepping scheme. Local time-step scaling.
3. Fourth-order filtering for both left- and right-hand side.
4. Baldwin-Barth 1-equation turbulence model.
5. The rotors are modeled by the momentum source model.

Rotor Model Supplements

This section describes some of the new features added to the momentum source model during the implementation in OVERFLOW-D:

1. Distribution of sources over several gridplanes in axial direction.
2. Blade tip force model.
3. Source term in the energy equation.

Distribution of Sources Over Several Gridplanes in the Axial Direction

The baseline hover case with a collective pitch angle of 38 deg is used for model testing and development. Figure 4 shows the axial speed change through the rotor disk at 75% of the rotor radius, computed with the momentum source model. The rotor forces are taken from a corresponding discrete blade solution⁴ and are held constant throughout the computation. The left of the figure is upstream of the rotor, and the z-coordinate is normalized to be zero at the rotor disk. Each square and diamond represents a gridpoint. The original model, shown as squares, applies the source terms at one grid plane. This leads to oscillations that extend nine gridpoints upstream and downstream of the rotor for all flow variables. The induced velocities some distance away from the rotor are not directly affected due to the conservative nature of the numerical scheme. The evaluation of angle-of-attack, however, and, therefore the forces on the rotor, are affected. The original model uses the speeds on the rotor source plane for evaluation of angle-of-attack. The axial speed has a peak at this gridpoint, leading to an under-prediction of angle-of-attack. This problem can be solved by averaging the flow quantities upstream and downstream of the oscillations for evaluation of angle-of-attack. The user can now specify a node increment giving the locations for flow averaging.

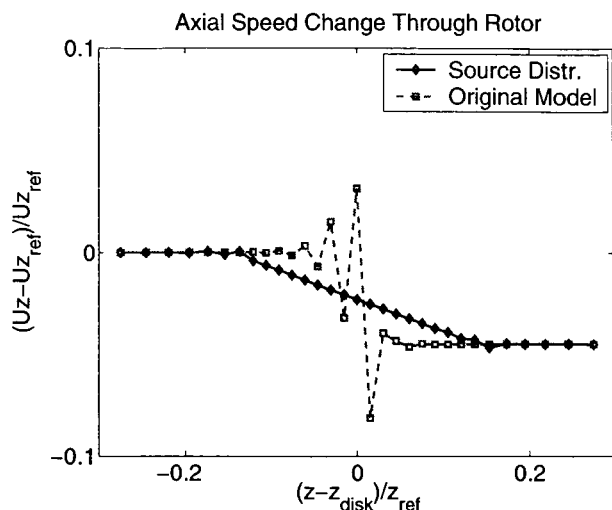


Fig. 4 Effect of source term distribution on axial speed, $r/R = 0.75$.

Another approach is to distribute the momentum sources in the axial direction. The diamonds in Figure 4 represent a solution where the source terms are equally spread out over 17 grid planes. A triangular shaped source distribution has also been implemented. Both the rectangular and triangular shapes of the axial source distributions produce smooth solutions. The flow quantities at the rotor plane are close to the averages of upstream and downstream values.

Figure 5 shows the tangential speed change through the rotor disk at 75% of the rotor radius. Behind the rotor, the tangential speed is 20% of the axial speed. The original model predicts 82% of this tangential speed at the rotor plane. Distribution of the sources

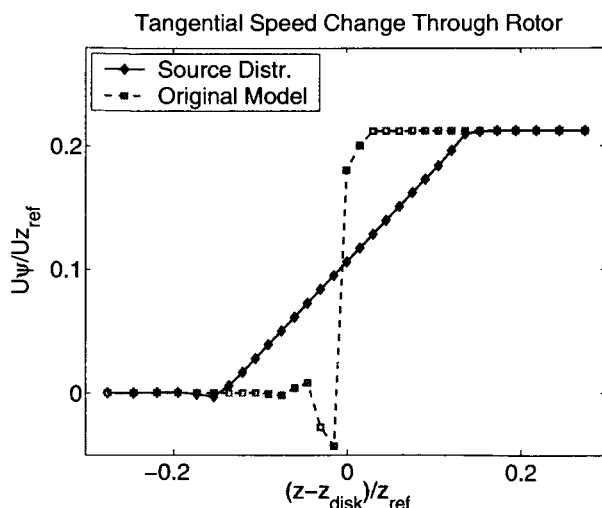


Fig. 5 Effect of source term distribution on tangential speed, $r/R = 0.75$.

result in a smooth profile, with a rotor disk tangential speed equal to 50% of the downstream tangential speed. Taking half the induced swirl behind the rotor into account when evaluating angle-of-attack is consistent with strip theory. This gives the best results for comparisons of momentum source and discrete blade solutions. The flow averaging method described above gives the same rotor plane tangential speed.

Figure 6 shows the change in angle-of-attack through the rotor disk at 75% of the rotor radius. The original model underpredicts the angle-of-attack

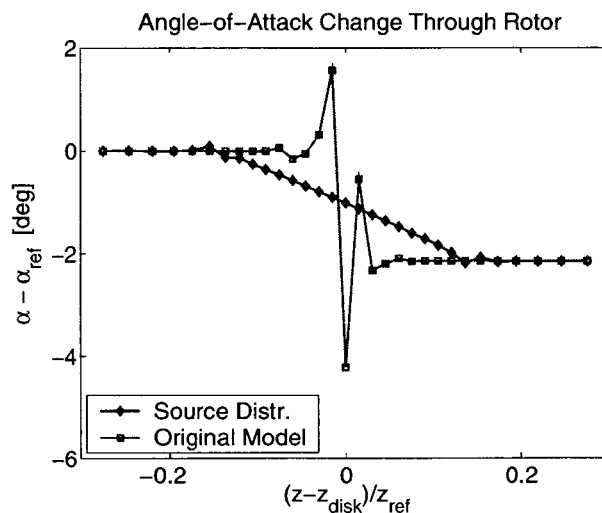


Fig. 6 Effect of source term distribution on angle-of-attack, $r/R = 0.75$.

by three deg at the rotor plane. In a fully coupled run this deviation will partly correct itself. The under-predicted angle-of-attack leads to lower rotor forces. This results in a reduction in induced velocities and an increase in angle of attack. Nevertheless, the axial distribution of the source term leads to a significant improvement in comparisons between the MSM and the DBM. The revised MSM predicts 2% lower thrust and 0.7% higher torque than the DBM. If we revert to applying momentum sources on a single grid plane, the total thrust is 18% lower, and the torque is 16% lower than the DBM for a fixed collective angle.

Blade Tip Force Model

A crucial element of the MSM verification is a comparison of MSM and DBM results for the RAH-66 Comanche FANTAILTM. The DBM results⁴ are also computed with OVERFLOW-D, and the comparison should therefore mainly show the effect of replacing the discrete blades with a MSM. The baseline case with collective pitch angle 38 deg is used for the comparison. The DBM solutions are averaged in the tangential direction. For each axial and radial position,

the solution variables of the DBM solution are interpolated to a circumferential gridline. The tangential spacing is uniform. Points that fall inside the blade geometry are removed from the average sample. In addition to the primitive variables, momentum fluxes such as $\rho U_z U_z$ and $\rho U_z U_\psi$ are averaged. The momentum fluxes are useful for comparisons of cases where the flow quantities vary significantly in the tangential direction, such as in the vicinity of a two-bladed rotor. If the time-averaged axial force spanwise distributions are the same for MSM and DBM, the axial momentum flux plus pressure should integrate to the same values over corresponding surfaces. If the time averaged tangential force spanwise distributions are the same for MSM and DBM, the product of angular momentum flux and radius should integrate to the same values over corresponding surfaces. The velocity and momentum profiles, however, may be different due to the nonlinear interaction between forces and induced velocities. For the eight-bladed RAH-66 Comanche FANTAILTM, the structure of the averaged momentum and momentum flux fields are similar, suggesting that the nonlinear effects of tangential variation are modest. The DBM flow field results are therefore presented in terms of straight averages.

Figure 7 shows the angle-of-attack and lift coefficient for the baseline case, computed with the DBM. However, the angle-of-attack in the DBM is not uniquely defined. For illustration purposes, the angle-of-attack is computed here from a flow field that is averaged in the tangential direction at the axial position of the pitch axis of the rotor blades. The axial speed is reduced 15%, to account for the speed-up

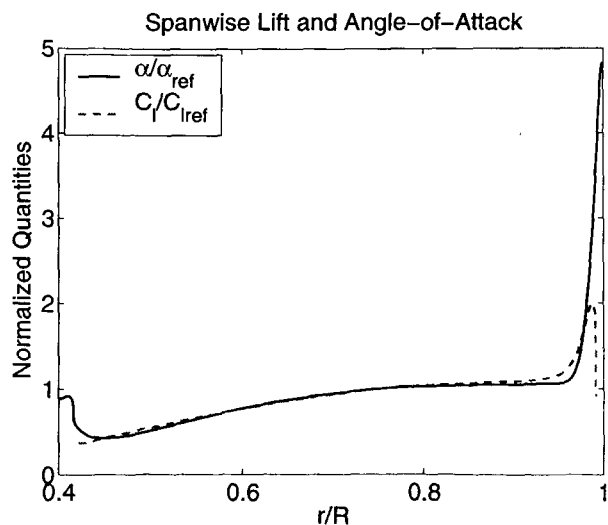


Fig. 7 Angle-of-attack and lift correlation, discrete blade model.

through the rotor due to the finite volume of the rotor blades. The swirl at the pitch axis is approximately 75% of the swirl in the rotor wake, and is reduced by one third, to bring it down to half the swirl in the rotor wake.

Figure 7 shows that the correlation between angle-of-attack and lift coefficient is good, except at the blade root and tip. At the tip, the angle-of-attack becomes very large, and the lift coefficient peaks at a value beyond $C_{l,max}$ in the two-dimensional (2D) airfoil table. The flow here is 3D, and the applicability of 2D airfoil tables becomes questionable.

A simple tip force model for ducted fan computations has been implemented in OVERFLOW-D, in order to reflect the 3D behavior close to the tip. The axial force per unit length of the blade for the tip region is obtained by linear extrapolation from a user defined reference radial position. We have used a reference position of 0.9R. The tangential force is evaluated from the axial force and the reference location axial and tangential forces in a manner that maintains the incremental rotor Figure of Merit towards the tip.

Figure 8 shows the axial force distribution computed with the DBM, the MSM/tip force model, and the original MSM model. The linear tip model does not capture the force peak at the tip completely, but it is a significant improvement over the original model. Due to the high angle-of-attack at the tip, the original MSM is stalled towards the tip, and therefore underpredicts the axial force. The rotor therefore draws less air over the shroud lip, reducing the shroud thrust. The axial speed through the duct decreases, which increases the angle-of-attack and increases the rotor thrust inboard of the tip.

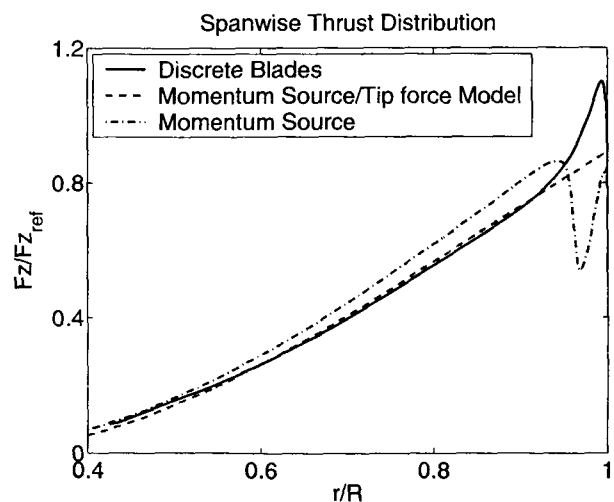


Fig. 8 Effect of tip force model on thrust distribution.

Figure 9 shows the tangential force distribution computed with the DBM, the MSM/tip force model, and the original MSM. The effect on the tangential force distribution is similar to the effect on the axial force distribution, with a somewhat larger difference between MSM and DBM.

The overall results improve significantly with the tip force model. Table 1 summarizes the results. The results are normalized by the discrete blade model results. The second line of the table shows the revised MSM model with all updates including the tip force model and the axial distribution of the sources. The results are in good agreement for the rotor thrust and torque and fair agreement for the duct thrust. The force peak at the blade tip draws more air over the shroud lip, giving higher duct thrust for the DBM. Line three shows the MSM results without the tip force model. The duct thrust is 22% lower than the DBM. The duct thrust appears to be sensitive to the details at the rotor tip. Line four shows the MSM results without axial distribution of source terms. All quantities are underpredicted due to the under-prediction of angle-of-attack. The original MSM was not designed for ducted fans, and differs significantly from the discrete blade model for all quantities.

Source Term in Energy Equation

The momentum source model was originally developed for an incompressible flow solver. In the compressible code OVERFLOW-D, the energy equation is the product of internal energy and the continuity equation plus the dot-product of the velocity vector and the momentum equation. Source terms in the momentum equation, therefore, carry over to the energy equation. The source term in the energy equation is the dot-

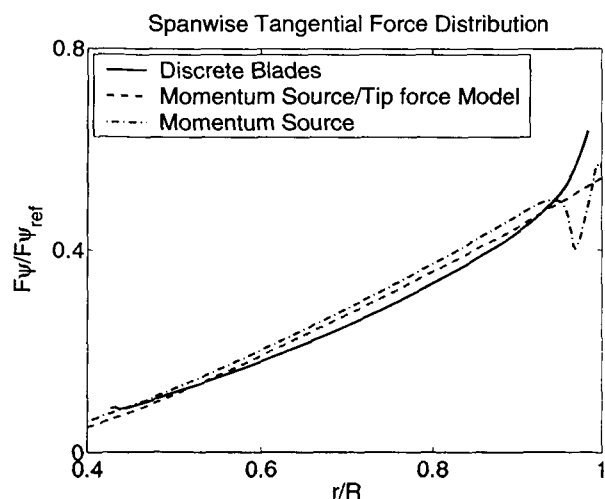


Fig. 9 Effect of tip force model on tangential force distribution.

product of the velocity vector and the source vector in the momentum equation.

Figure 10 shows the stagnation enthalpy downstream of the rotor. The computation with energy source term clearly improves the stagnation enthalpy profile. The effects on the velocity and pressure fields are small due to the modest Mach number for this case.

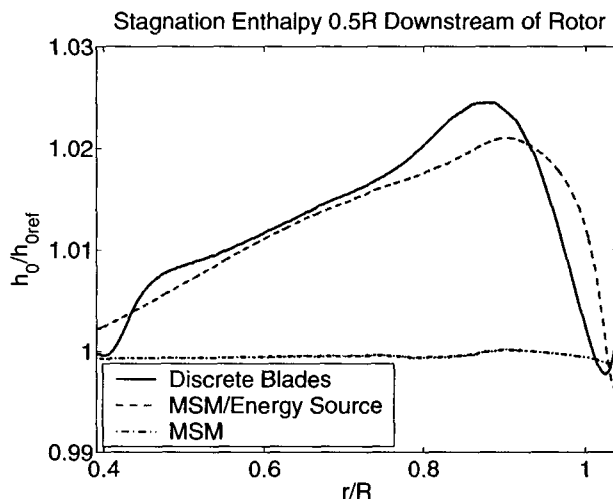


Fig. 10 Effect of energy source term on stagnation enthalpy.

Solution Procedure and Grid Convergence for MSM Computations

OVERFLOW-D computes axisymmetric cases by solving on three gridplanes and by applying periodic boundary conditions in the azimuthal direction. The baseline grid system has approximately 100 grid points around the shroud, and approximately 100 gridpoints around half the hub. The hub and shroud grids have viscous wall spacing corresponding to a y^+ of one. The stretching ratio in surface normal direction has a maximum of 1.3. The spacing in the axial direction at the rotor plane is 0.001R.

The radial spacing of the rotor grid corresponds to y^+ of one on the shroud wall, stretching to 0.001R through twice the thickness of the tip gap. The momentum source tip gap (i.e. no sources added) corresponds to the physical tip gap of the discrete blade rotor. The maximum radial spacing at mid-span is 0.03R. The rotor grid has 81 grid points in radial direction and 37 grid points in axial direction. The source terms are applied over 9 grid points in axial direction. The automatic generation of offbody grids in OVERFLOW-D is not used for the axisymmetric computations. Instead, one single box grid with variable

Table 1 Effect of model supplements on overall forces and moments.

Model	Normalized Forces and Moments		
	Rotor Thrust	Shroud Thrust	Torque
Discrete blade model	1.0	1.0	1.0
MSM	0.99	0.96	0.99
MSM w/o tip model	1.03	0.78	1.02
MSM w/o axial dist	0.82	0.81	0.84
Original MSM	0.84	0.69	0.86

spacing is used as background grid. The grid spacing is constant $0.045R$ in a subdomain extending $1.5R$ upstream, $2R$ downstream and $2R$ to the side of the rotor center. The maximum stretching ratio outside this subdomain 1.3 . The domain size extends $5R$ upstream, $5R$ downstream and $5R$ radially from the rotor center. Extending the domain size up to $12R$ from the rotor center does not affect the computed overall forces.

The baseline grid system has approximately 17,000 near-body and 11,000 off-body grid-points for each of the three grid planes. A corresponding 3D case would typically have six million near-body gridpoints and roughly the same number of offbody grid points. The baseline grid described above was obtained by removing every other point from a finer grid system.

The duct thrust, fan thrust and torque computed with these two grid systems deviated by less than two percent. In addition, separate computations with extreme resolution for: 1) the rotor grid; 2) the shroud wall region and 3) the offbody grids revealed no significant changes in overall forces or wake structure. Axisymmetric computations enable quick grid refinement studies with resolution well beyond what is possible with 3D computations. The baseline grid system was shown in the section on Computational Model Description.

The hover computations are started with the full tip-speed and potential theory lift $C_l = 2\pi\alpha$, with no limits on the lift. With zero induced velocity, the angle-of-attack corresponds to the twist distribution. For high α and airfoil stall, potential theory lift is significantly higher than the lift from the airfoil tables. This quickly establishes the induced flow field. The computations are restarted after 1000 time-steps with airfoil look-up tables for the aerodynamic forces.

Jacobian time-step scaling is used to accelerate convergence towards steady-state solutions. A convergence history for the forces is shown in Figure 11. The quantities are normalized by the end values. The high frequency oscillations are caused by vortex shedding from the base of the shroud. The bottleneck for the convergence is the wake position moving relatively slowly towards the axis of rotation. A solution can typically be obtained with 20000 time steps. This takes

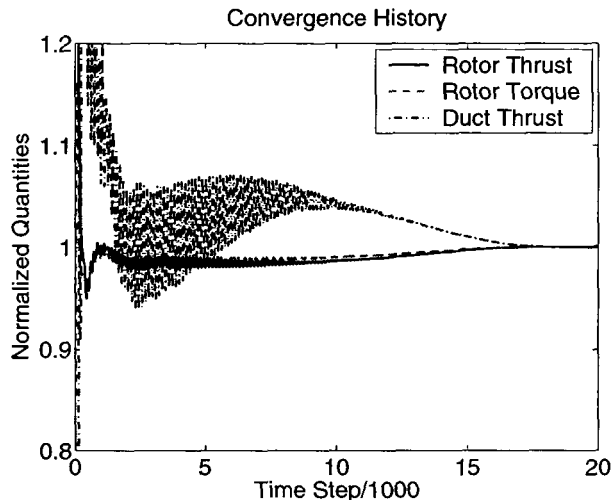


Fig. 11 Convergence history for thrust and torque.

two hours on a single 450 MHz processor, which makes it well suited for initial design and optimization studies.

Results

The baseline hover case with collective pitch angle 38 deg is used for a detailed comparison of MSM and DBM results. The DBM solutions⁴ are averaged in the tangential direction for comparison with the MSM results as described earlier. Figure 12 shows a comparison of axial momentum. The inlet to the fan is facing up on the figures. The axial location of the rotor corresponds to the maximum thickness of the shroud. Negative momentum is directed downwards. Dark blue indicates zero or reversed (upwards) flow. The axial momentum above the rotor is in good agreement. At the rotor there are differences due to the three-dimensional nature of the discrete blade solution. For both models, the flow separates at the shroud wall slightly upstream of the rotor. This is due to the tip vortices lifting the flow away from the wall. The adverse pressure gradient in the diverging duct downstream of the rotor prevents the flow from reattaching. The main features of axial speed are in good agreement for the two different modeling approaches.

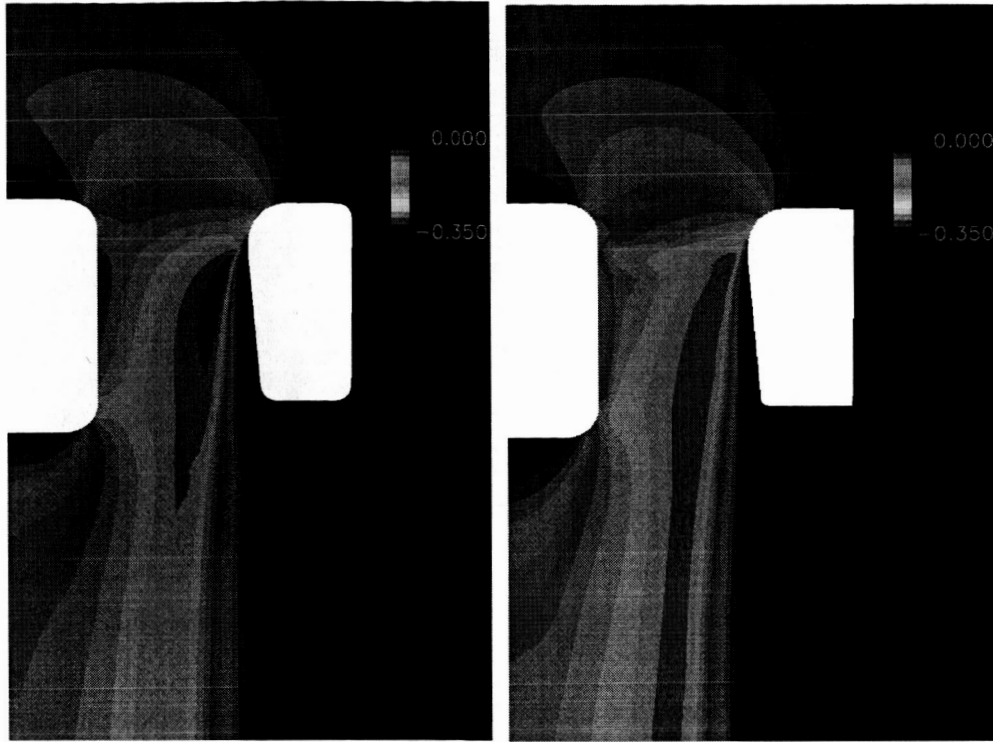


Fig. 12 Comparison of normalized axial momentum for MSM(left) and DBM(right).

Figure 13 shows the radial distribution of axial speed 0.15R upstream of the rotor. The MSM predicts slightly higher speed towards the hub. This is due to the simplified modeling of the blade close to the hub in the MSM, where the two-dimensional airfoil tables and the full chord length are applied all the way to the hub. The DBM has free-floating blades with a gap between the hub and the blade root.

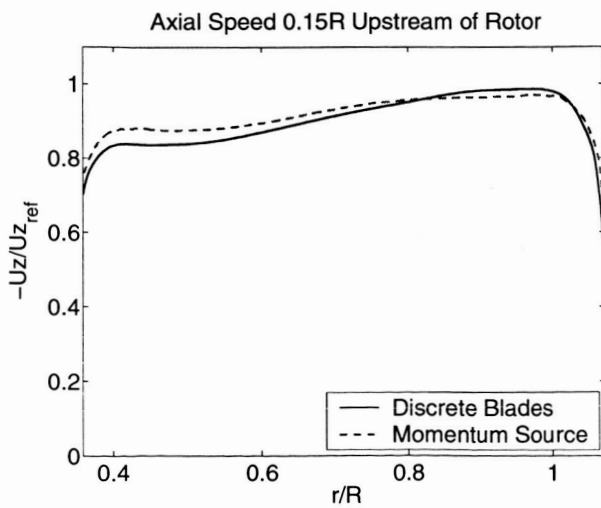


Fig. 13 Normalized axial speed distribution upstream of rotor.

Figure 14 shows the axial speed at a plane going through the rotor pitch axis. The axial speed is somewhat higher, in particular towards the hub for the DBM. Approximately 15% of the rotor plane area is here inside the rotor geometry. This gives higher speeds through the rotor for the DBM than for the MSM.

Figure 15 shows the radial distribution of axial speed

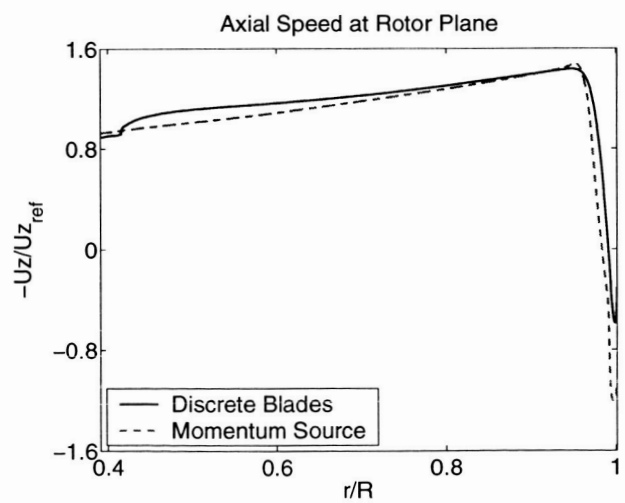


Fig. 14 Normalized axial speed distribution in rotor plane.

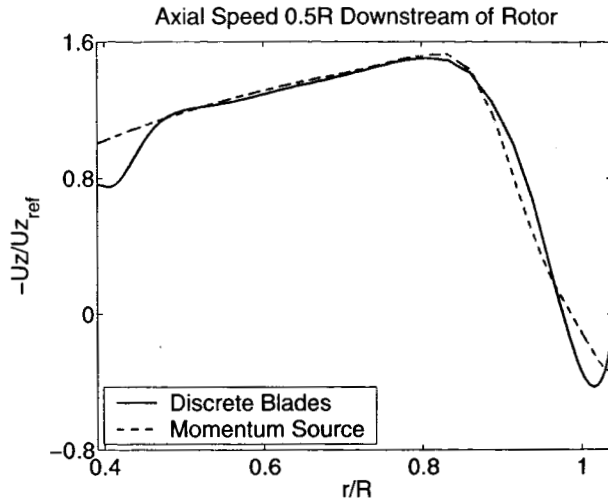


Fig. 15 Normalized axial speed distribution downstream of rotor.

0.5R downstream of the rotor. They are in good agreement except at the root and tip. At the hub, the MSM predict higher speed, due to over-prediction of forces towards the hub. The reversed flow layer towards the rotor tip is thicker and has higher mass flow for the DBM, which is compensated by higher speed outside the reversed flow layer.

Figure 16 shows a comparison of tangential speed. Both models predict approximately the same strength of the hot spot, approximately one quarter of the tip speed. MSM predicts the position slightly upstream of the DBM prediction. The abrupt onset of swirl at the rotor disk for the MSM is due to the short axial extent of the source terms and the lack of circulation associated with discrete blade lift. MSM has higher swirl at the hub than DBM due to the zero root gap in the MSM. This also causes accumulation of swirl in the wake of the hub for the MSM. One significant difference between the models is the mixing of swirl into the reversed flow region for the MSM, especially on the hub.

The tangential speed 0.5R downstream of the rotor is shown in Figure 17. The overall patterns agree well, but there are significant differences at the tip and root. The MSM lacks the root vortex system altogether, and has only a vortex sheet at the tip. The DBM has discrete tip vortices traveling down the shroud. The DBM vorticity vectors have axial components, and therefore they influence the tangential speed profiles. It is not surprising that the complex reversed flow shroud boundary layer is computed differently by the two models.

Figure 18 shows a comparison of stagnation enthalpy. The hot spots for stagnation enthalpy are lo-

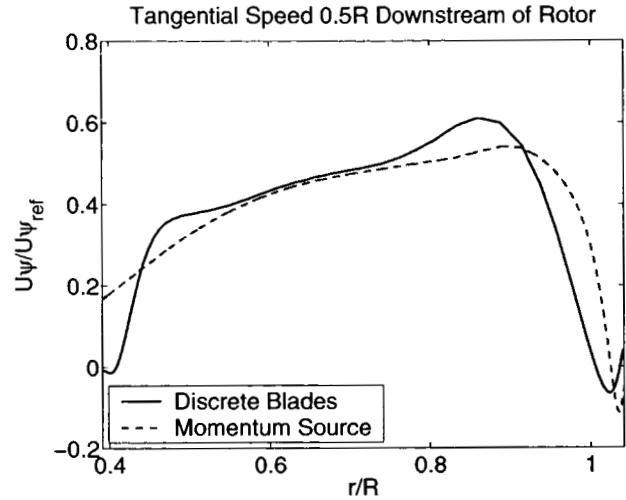


Fig. 17 Normalized tangential speed distribution downstream of rotor.

cated at the positions for zero axial speed. Here work is performed on air that is not transported away, resulting in a build-up of stagnation enthalpy. The patterns of the two models are in good agreement. MSM performs work on the air all the way to the hub, where the discrete blades hardly interact with the flow. In the reversed flow zone on the shroud wall, the MSM has higher swirl, resulting in higher stagnation enthalpy here.

Figure 19 shows the radial distribution of stagnation enthalpy 0.5R downstream of the rotor. The overall patterns are in good agreement. Again, the differences at the root and tip are probably caused by the root and tip vortices in the discrete blade model.

Figure 20 shows a comparison of normalized pres-

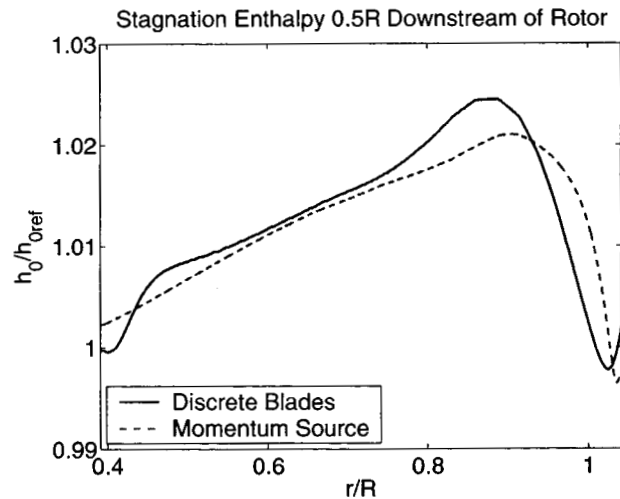


Fig. 19 Normalized stagnation enthalpy distribution downstream of rotor.

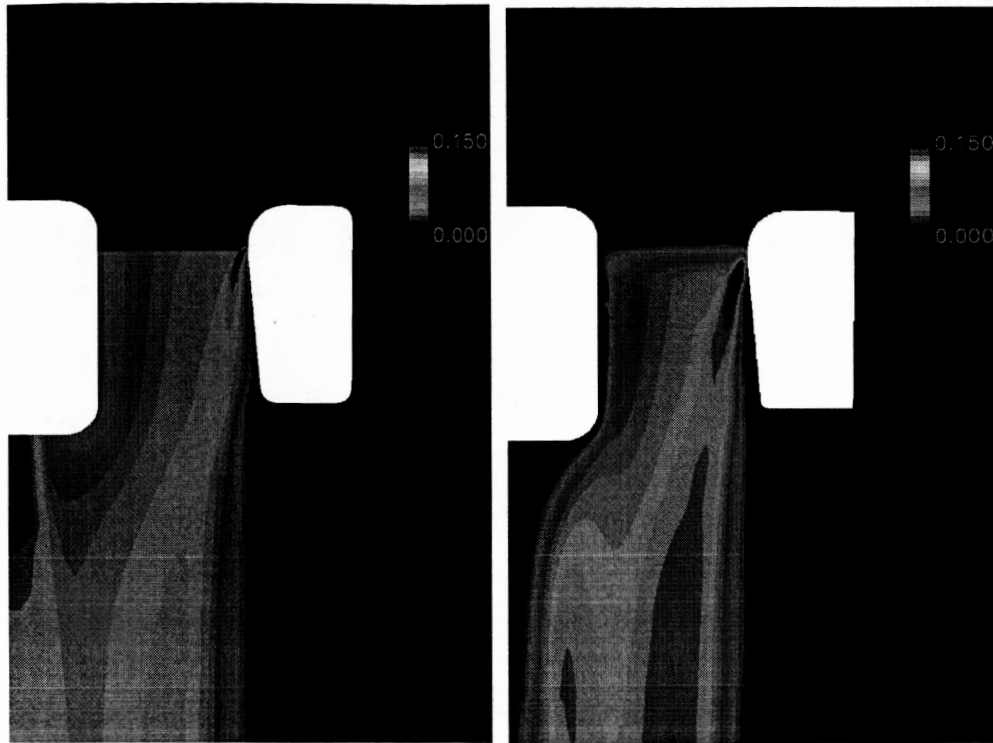


Fig. 16 Comparison of normalized tangential momentum for MSM(left) and DBM(right).



Fig. 18 Comparison of normalized stagnation enthalpy for MSM(left) and DBM(right).

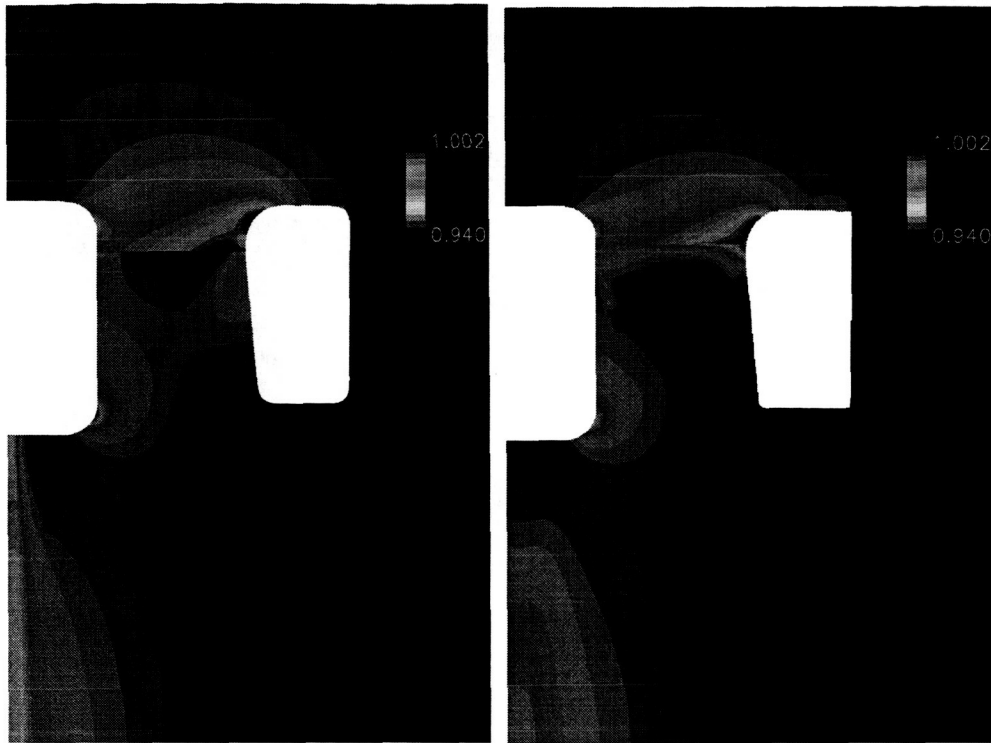


Fig. 20 Comparison of normalized pressure for MSM(left) and DBM(right).

sure. The overall patterns are in good agreement. The abrupt pressure change through the MSM rotor disk is due to the shorter axial extent of the momentum sources than the axial extent of the pitched discrete blades. Away from the rotor disk, however, the pressure fields are similar. Radial distributions of rotor blade forces, and overall forces and moments were shown earlier in the section on model modifications.

The sensitivity to tip gap is illustrated in Figure 21. If the tip gap is reduced 50%, the leakage back through the gap and the thickness of the reversed flow zone is reduced. This increases the mass flow and the thrust from the shroud lip. The increased speed through the rotor reduces the angle-of-attack, and the rotor thrust and torque decrease. The net effect is an increase in thrust and a decrease in torque, and FM increases 10%. This translates to a seven percent increase of thrust for the same torque.

The thrust augmentation factor, γ , is defined as total thrust divided by fan thrust. It can theoretically reach a value 2.0 for a ducted fan, which means that the fan and duct contribute equally to the total thrust. Figure 22 shows the sensitivity of the thrust augmentation factor to the tip gap. At the nominal tip gap, γ for both MSM and DBM(not shown) are 85% of the experimental γ . One possible cause for the difference may be exaggerated reversed flow zones for the CFD

models.

CFD models tend to smear out vortices due to numerical diffusion, which could lift the shroud boundary layer too far away from the wall at the rotor. Computation of the wall layer thickness downstream of the rotor is sensitive to the exchange of momentum between the two opposing flows. This requires grids that

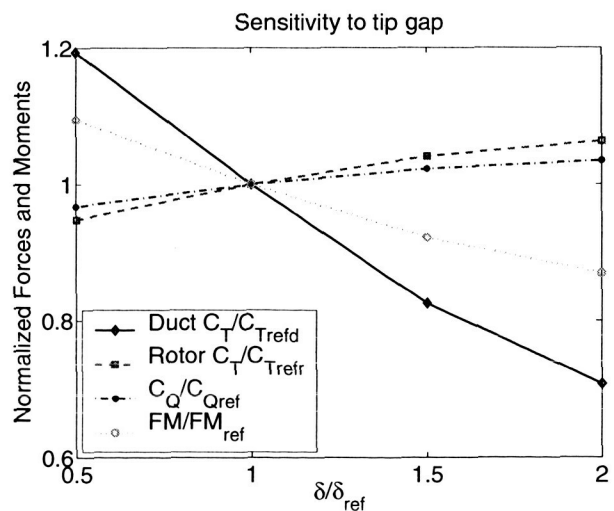


Fig. 21 Sensitivity of forces and moments to tip gap.

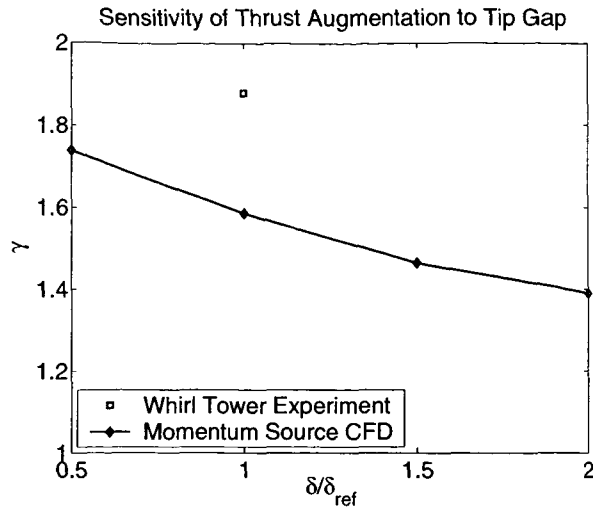


Fig. 22 Sensitivity of thrust augmentation to tip gap.

adequately resolve the flow features of this shear layer, and probably more realism and accuracy in the turbulence modeling than we have at hand today. The computed thrust augmentation factor increases 9% if the tip gap is reduced 50%.

Figure 23 shows total thrust vs. torque for the Boeing and Sikorsky experimental data sets mentioned earlier and the DBM and MSM computations. The DBM results are for collective pitch angles 8, 18, 28 and 38 deg. The momentum source results are for collective pitch angles -20, -10, 8, 18, 28 and 38 deg. The differences for corresponding CFD DBM and MSM data points are consistent with the 38 deg case analyzed in detail above. There is a systematic shift of the results between the two experimental data sets of

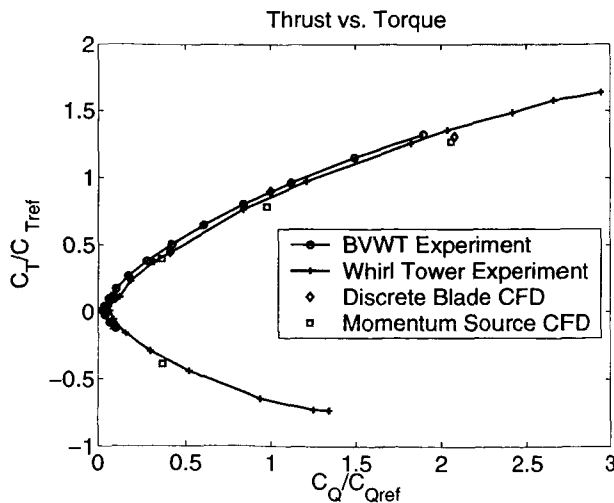


Fig. 23 Thrust vs. torque collective-sweep.

about five percent of the thrust at 38 deg collective angle. Given the geometric differences between the two wind tunnel models (including the tip gaps), the results agree remarkably well, giving confidence in the data.

The CFD models add yet another interpretation of the geometry and run conditions. The information about the tip gap is available as an interval, bounded by measured values on any individual blade. The CFD tip gap is simply the midpoint in this interval. The DBM results (thrust for a given torque) differ from the measured data by maximum five percent. The MSM results differ from the measured data by maximum seven percent. This may well be within the variation caused by different tip gaps for CFD and experiment combined with experimental uncertainty. We therefore conclude that CFD and experiment are in good agreement for thrust vs. torque.

Conclusions

A Momentum Source Model (MSM) that was originally developed for unducted rotor computations has been implemented and developed further in the flow-solver OVERFLOW-D.

In a hierarchical modeling approach, Discrete Blade Model (DBM) results for the RAH-66 Comanche FANTAILTM have been used extensively for validation and development of the MSM for ducted fan computations. This proved to be crucial for addressing issues specific to ducted fan computations.

The most important model revisions include axial distribution of the source terms and a new tip force model for ducted fans.

The model revisions improve the results significantly. The baseline hover case for comparison of the models has a collective pitch angle of 38 deg. The rotor thrusts for the original and new MSM are 84 and 99% of the DBM rotor thrust, respectively. The duct thrusts for the original and new MSM are 69 and 96% of the DBM duct thrust, respectively. The torques for the original and new MSM are 86 and 99% of the DBM torque, respectively.

Comparisons between MSM and DBM flow fields are carried out by averaging the DBM results in the tangential direction. The main flow features are in good agreement except close to the rotor disk. MSM is, therefore, a good option when details in the immediate vicinity of the rotor are not the primary priority. Overall torque and thrust agree well for the computed collective pitch angles between 8 and 38 deg. The differences are mainly due to a force peak at the blade tip due to the tip vortex system. This effect is only partially captured with the tip force model in the MSM.

The MSM results are sensitive to the chosen tip gap.

A tip gap reduction of 50% increases the Figure of Merit ten percent, and the thrust augmentation factor nine percent.

Both MSM and DBM results agree well with experimental data for thrust vs. torque. They are systematically predicting lower thrust for a given torque than the experimental results. The differences may well be within the uncertainty due to selection of the CFD tip gap combined with the experimental uncertainty.

The new MSM offers a good complement to DBM for ducted fan computations. The lower computational and labor costs make parametric studies, optimization studies and interactional aerodynamics studies feasible for cases beyond what is practical with a DBM today.

Acknowledgements

This work was funded by the Aeroflightdynamics Directorate, US Army Aviation and Missile research, Development and Engineering Center through the Contract NAS2-00062 to ELORET. The pressure disk/MSM was obtained from Mr. Mark S. Chaffin at Langley Research Center. Dr. Gene Ruzicka, U.S. Army Aeroflightdynamics Directorate at Ames Research Center provided the discrete blade RANS results. Dr. Roger Strawn, U.S. Army Aeroflightdynamics Directorate at Ames Research Center contributed with many helpful and interesting discussions. Mr. Mark Potsdam, U.S. Army Aeroflightdynamics Directorate at Ames Research Center provided excellent support on OVERFLOW-D during the implementation of the MSM. Mr. Chuck Keys, Mr. Roger Lacy and Mr. Peter Christis of Boeing supported the application of FANTAILTM CFD modeling. Dr. Ganesh Rajagopalan of Iowa State University participated in discussions of the suitability of CFD to model FANTAILTM performance.

References

- ¹Rajagopalan, R. G., and Keys, C. N., "Detailed Aerodynamic Analysis of the RAH-66 FANTAIL using CFD," *Journal of the American Helicopter Society*, Oct. 1997, pp. 310-320.
- ²Alpman, E., Long, L. N., and Kothmann, B. D., "Unsteady RAH-66 Comanche Flowfield Simulations including Fan-in-Fin," AIAA Paper 2003-4234, June 2003.
- ³Chaffin, M. S., and Berry, J. D., "Navier-Stokes Simulation of a Rotor using a Distributed Pressure Disk Model," American Helicopter Society 51st Annual Forum, Fort Worth, TX, May 1995.
- ⁴Ruzicka, G. C. and Strawn, R. C., "Discrete Blade CFD Analysis of Ducted Tail Fan Flow," AIAA Paper 2004-48, Jan. 2004.
- ⁵Vuillet, A., and Morelli, F., "New Aerodynamic Design of the Fenestron for Improved Performance," 12th European Rotorcraft Forum, Garmisch-Partenkirchen, FRG, Sept. 1986.
- ⁶Robinson, F., "Increasing Tail Rotor Thrust and Comments on Other Yaw Control Devices," *Journal of the American Helicopter Society*, Oct. 1970, pp. 46-52.

⁷"BVWT 0345: Wind Tunnel Test on the 0.75 Scale L.H.X. Fan-in-Fin Powered Model," Boeing Report 8-7891-1-882, March 1990.

⁸"RAH-66 Demonstration/ Validation Fantail Rotor Whirl Test Report," Boeing Sikorsky Document 2000-224-001, Nov. 1996.

⁹Meakin, R. L., "Automatic Off-Body Grid Generation for Domains of Arbitrary Size," AIAA Paper 2001-2536, June 2001.

¹⁰Meakin, R. L., "Adaptive Spatial Partitioning and Refinement for Overset Structured Grids," *Comput. Methods Appl. Mech. Engrg.*, Vol. 189, No. 1077-1117, 2000.

¹¹Buning, P. G., Jespersen, D. C., Pulliam, T. H., Chan, W. M., Slotnik J. P., Krist, S. E., and Renze, K. J., *OVERFLOW User's Manual, Version 1.8*, NASA Langley Research center, Hampton, VA, 23681-0001, 1998.